Supplementary Information to: "A tale of two antennules: The performance of crab odor-capture organs in air and water"

Lindsay D. Waldrop[1], Laura A. Miller[2], and Shilpa Khatri[1]

[1]Applied Math Unit, School of Natural Sciences, University of California, Merced, CA, USA

[2]Depts. of Biology and Mathematics, University of North Carolina, Chapel Hill, NC, USA

In this supplement, we provide further details on the materials and methods used to obtain the results presented in the paper, "A tale of two antennules: The performance of crab odor-capture organs in air and water". In what follows, we begin by providing the methodology used to measure flow on physical models of the crab antennules using particle image velocimetry. Further, we provide the details of the mathematical model and numerical method used to conduct the computational simulations, including how the experimental velocity fields were coupled with the model. Finally, we give details on how the presented results were standardized and the statistical analysis.

Also, included in this supplement are movies of simulations which correspond to results presented in Fig. 4 in the paper.

Measuring flow on dynamically scaled physical models

Dynamically scaled physical models

The dynamically scaled physical models of the crab antennules were used in previously published studies. These papers contain additional details on the construction of the models [1, 2, 3]. These physical models were created using previously collected morphometric measurements on the antennules of the marine blue crabs, *Callinectes sapidus* Rathburn 1896, [1, 3] and the terrestrial hermit crab, *Coenobita rugosus* Milne-Edwards 1836 [4, 3, 2]. Each model consisted of a Sculpey Premo! clay flagellum (Polyform Products Co., Elk Grove Village, IL) in which glass rods were inserted to mimic the number, arrangement, and insertion angle of the real aesthetascs. The glass rods were clear, borosilicate glass (blue crab: Pyrex brand, hermit crab: Kugler-Color brand). For the blue crab, clear borosilicate glass was heated over a Bunsen burner and hand-pulled to match the diameter of each aesthetasc then cut to the appropriate length. For the hermit crab, clear borosilicate glass was hand-shaped with glass-working tools over a flame-working torch to the appropriate width, thickness, and length. The models were then cured at 80 °C for 40 to 45 mins (based on the thickness of the clay flagellum).

Two models were constructed of the blue crab antennule to measure steady-state motion: (1) aesthetascs spread apart (splay ratio = 2.19) to mimic the 'splayed' orientation of the aesthetascs during the downstroke in water, and (2) aesthetascs relatively clumped together (splay ratio = 1.66) to mimic the 'clumped' orientation of the aesthetascs during both the

return strokes in air and water and the downstroke in air (see section below justifying this choice and defining splay ratio). The models of blue crabs were scaled up 70 times the original size of the aesthetasc-bearing region of the flagellum (2 mm on the real animal). Only one model was constructed of the hermit crab antennule since the aesthetascs do not change configuration between the downstrokes and return stroke. The model was scaled to the original size of the antennule of a typical terrestrial hermit crab.

Dynamic similarity was accomplished by matching the Reynolds numbers (Re) of the real and modeled antennules during flicking:

$$Re = \frac{Ud\rho}{\mu}, \tag{1}$$

where d is the aesthetasc diameter, U is the speed of the stroke, ρ is the fluid density, and μ is the dynamic viscosity of the fluid. Since the aesthetasc diameters were scaled up, we used a fluid with greater viscosity, mineral oil: $\rho = 840$ kg m^{-3} and $\mu = 0.049 \pm 0.002$ Pa s (SD, $n = 3$), and altered speeds (U) to match the Reynolds numbers. The Reynolds numbers used for simulating the downstroke and return stroke in air and water are listed in the paper in Table 1 for the terrestrial hermit crab and Table 2 for the marine blue crab. Speeds measured on the models were converted to animal-relevant speeds for use with the mathematical model.

Particle Image Velocimetry

Full details of the tank system used to collect data by particle image velocimetry (PIV) are available in Loudon et al. [5]. The models were, one at a time, submerged in a tank (size: 50 cm by 50 cm by 100 cm) of mineral oil that was seeded with reflective glass spheres (diameter = 11 μm). Each model was mounted to a rail system with a camera (MotionScope PCI 1000s camera; Red- lake, Inc., Tucson, AZ), positioned directly above the model. A plane of laser light (thickness: 3 mm) was used to illuminate a narrow section of the tank that bisected the model. The camera-model apparatus was moved on the rail system parallel to the long axis of the tank by a stepper motor controlled by MATLAB (single-axis micro-stepping positioning system MC6023; Daedal, Inc., Irwin, PA), at a steady speed matching the appropriate speed based on the Reynolds number. The model moved through the oil and the camera captured sequential images of the model and the movements of the reflective particles. The refractive indices of the borosilicate glass used to model the aesthetascs (1.47) was very close to that of the mineral oil (1.46), allowing for visualization of fluid movement within the aesthetasc array without distortion.

Pairs of sequential images were then processed with MatPIV v1.6.1 [6] based on the method presented in Cowen and Monismith [7]. Images were divided into sub-windows of 8×8 pixels and cross-correlation algorithms calculated the probable displacements of particles within each sub-window. Dividing these displacements by the time step between frames (1/60 s) resulted in a velocity vector for each sub-window of the domain. Velocity vectors were then filtered and interpolated on thresholds based on nearest-neighbor and full-domain comparisons.

Sixty image pairs were processed this way, then the velocity vectors for each sub-window were averaged to give a mean steady-state velocity field for each run within the tank. This process was repeated three separate times for each model at each orientation and for each velocity to create three unique repetitions for every set of conditions.

Wall Effects

To minimize the wall effects of translating a physical model within a finite-volume tank at low Reynolds numbers, we sized the model according to a commonly used rule-of-thumb relation between the size of the model and the size of the tank [5]. If,

$$\frac{y_w}{L_f} > \frac{20\nu}{L_f U_b}, \tag{2}$$

where L_f is the diameter of the flagellum at its widest point, y_w is the distance between the wall and the outer edge of the model at its widest point, U_b is the speed of the model relative to the wall, and ν is the kinematic viscosity of the fluid, then wall effects are small enough to be safely ignored. Our models were farther than the minimum required distances ($y_w = 0.06$m) so wall effects were ignored (see [1, 2] for calculations for each species model).

Justification for using steady-state flow to estimate the velocity field during a flick

Although the motion of the antennule is unsteady, we used steady-state flow fields measured by PIV for our numerical model as an approximation of the actual flow fields since periods of accelerations are short. To justify this approximation, we use the Womersley number, Wo, which is a non-dimensional number that describes the relative importance of unsteady features of the fluid flow:

$$Wo = 0.5L\sqrt{\frac{2\pi f}{\nu}}, \tag{3}$$

where L is a characteristic length, f is a periodic frequency, ν is the fluid's kinematic viscosity [5]. $Wo < 1$ indicates that inertia of pulsing flow is quickly damped out by the fluid viscosity, and unsteady effects are negligible. Using $L = 8.9 \times 10^{-6}$ m, $f = 24$ Hz and the fluid density and viscosity reported in the paper in Table 1, we find that for for terrestrial crabs $Wo \approx 0.01$. Using the values in Table 2, we find that for marine crabs, $Wo \approx 0.05$. These values are well below $Wo = 1$, indicating that unsteady effects are minimal [1].

Justification for using the 'clumped' aesthetasc arrangement during the downstroke of marine crabs in air

The aesthetascs of blue crabs are long and flexible compared to many other malacostracan crustaceans, including the terrestrial hermit crabs in the *Coenobita*. During the downstroke of flicking in water, these long, flexible aesthetascs splay away from each other due to passive hydrodynamic drag [1, 4]. The splay of aesthetascs increases water penetration of the array during the downstroke [1]. We will consider the effect of displacement by calculating the splay ratio consistent with what is reported during flicking. The splay ratio is the width of the array measured at the distal tips of the aesthetascs divided by the width of the array at the point of hair insertion into the flagellum.

Air is considerably less dense than water, and it is worth considering whether or not aesthetascs of the blue crabs would splay to the same degree during flicking as they do in water. To estimate aesthetasc splay, we use a model presented in Waldrop [4]. The effects of the ontogenetic scaling of array morphometrics and flicking kinematics are used to estimate aesthetasc splay. The model is based on a fixed cantilever bending equation.

For a crab in water, the splay ratio during the downstroke was 2.2, very close to measured values for *H. oregonensis* individuals of this body size reported in [4]. For the calculation of

splaying in air, ρ was set to 1.225 kg m^{-3}. As a result of the large difference in density, the calculated splay ratio was 1.002, indicating that no meaningful splay takes place during the downstroke in air. We then assumed that the aesthetasc array of the blue crab would not splay apart during the downstroke in air. We used velocity fields measured by PIV on the dynamically scaled physical model of a clumped array at the downstroke speed.

Positioning of aesthetascs in the PIV velocity fields

Since the glass aesthetascs were transparent in the PIV images, the positions of the aesthetascs are not obvious. The splayed models of *C. sapidus* and *C. rugosus* were were placed in a clear-bottom tank of mineral oil. The models were positioned such that the oil-air interface captured the same cross-section of the model as the laser used to capture PIV data, thus individual aesthetascs were clearly outlined at each interface by the meniscus of the oil. The models were photographed from below so that the edges of the glass aesthetascs were visible relative to the model flagellum (for more details, see [1]).

For the clumped model of *C. sapidus*, the positions of the aesthetascs were not consistent in number or relative position with the splayed model. Because we are interested in modeling 2D flow, we chose to reposition the aesthetascs of the splayed model to fit the data of the clumped model. To do this, photos of the splayed model and clumped model in air were taken to determine the relative position of the edges of the array. The edges of the photograph of the splayed model were then linearly transformed to the edges of the clumped model using MATLAB's image processing package. The transformation object created during this process was used to transform the positions of the splayed aesthetascs to the positions used for the clumped model.

Computational Model

Mathematical Model

The advection-diffusion equation (in conservative form) for the odor concentration, $C(x, y, t)$, is solved

$$\frac{\partial C}{\partial t} + \frac{\partial (uC)}{\partial x} + \frac{\partial (vC)}{\partial y} = D\left(\frac{\partial^2 C}{\partial x^2} + \frac{\partial^2 C}{\partial y^2}\right), \tag{4}$$

in a given domain Ω with the steady-state velocity fields taken from PIV data, (u, v).

Within Ω there are a number of aesthetascs, and their locations are shown in the graph of the PIV data (see Figs. 2 and 3 in the paper). At each timestep, the odor concentration within the aesthetascs was set to 0, modeling the absorption of those odor molecules.

Choosing the domain

Four sets of PIV data have been used, marine and terrestrial crabs, both in water (Re_{water}) and in air (Re_{air}), with three replicates of each. Two PIV velocity fields have been collected for each case, giving the downstroke and return stroke vector fields and the location of the aesthetascs. The velocity field data are not perfectly aligned between the downstroke and return stroke. For the simulations, the fields required realignment in order to connect the downstroke seamlessly with the return stroke and the rest period. One domain for each case was chosen to allow for this using the following steps:

1. Find the center of all of the aesthetascs during the downstroke and the return stroke velocity fields. Determine the appropriate shift that is needed to align the return stroke velocity field with the downstroke velocity field. In some cases, the velocity fields were already perfectly aligned.

2. Find the largest rectangle that can fit interior to both velocity fields (the downstroke velocity field and the shifted return stroke velocity field).

3. Note that the domain chosen for the simulation, Ω, is then slightly smaller in both directions to allow for extrapolation for the advection boundary conditions.

This procedure resulted in the following domain sizes for each case with three replicates: marine crabs with Re_{water} were simulated in 2.19×1.91 mm^2, 2.19×1.91 mm^2, and 2.18×1.86 mm^2 domains, marine crabs with Re_{air} in 2.18×1.86 mm^2, 2.18×1.86 mm^2, and 2.18×1.86 mm^2 domains, terrestrial crabs with Re_{air} in 0.21×0.19 mm^2, 0.23×0.19 mm^2, and 0.21×0.19 mm^2 domains, and terrestrial crabs with Re_{water} in 0.22×0.19 mm^2, 0.23×0.19 mm^2, and 0.22×0.19 mm^2 domains.

Initial Conditions

Two different initial conditions for the chemical gradient are used in the simulations. The first initial condition is a thin filament of odor whose concentration has an exponential profile,

$$C(x, y, 0) = C_\infty e^{-7(2(x-x_c)/0.1)^2}, \tag{5}$$

with a width of 0.1 mm centered at x_c. We standardize the distance from the farthest right point on an absorbing aesthetasc to be 0.0125 mm from the left most point within the filament to determine x_c. We also standardize the total amount of chemical present (integration in x and y on the domain) by modifying the maximum value of the concentration, $C_\infty = 0.1/Ly$, where Ly is the domain length in the y-direction (given above for each case). The second initial condition, the thick filament, is a never-ending filament in relation to the simulation. This initial odor concentration has the same exponential profile, Eq. 5 as in the first condition from $x_c - 0.05$ mm to x_c and then $C(x, y, 0) = C_\infty$ for $x > x_c$.

Numerical Methods

The mathematical model was solved numerically using the following steps to advance one timestep:

1. First, for half a timestep the odor concentration was advected by solving,

$$\frac{\partial C}{\partial t} + \frac{\partial (uC)}{\partial x} + \frac{\partial (vC)}{\partial y} = 0\,. \tag{6}$$

2. Then the concentration was diffused a full timestep by solving,

$$\frac{\partial C}{\partial t} = D\left(\frac{\partial^2 C}{\partial x^2} + \frac{\partial^2 C}{\partial y^2}\right)\,. \tag{7}$$

3. Then it was noted how much concentration had reached each grid point within an aesthetasc and the concentration was set to 0 at that grid point.

4. Then again the concentration was advected another half timestep

$$\frac{\partial C}{\partial t} + \frac{\partial (uC)}{\partial x} + \frac{\partial (vC)}{\partial y} = 0\,. \tag{8}$$

Strang splitting allows for the partial differential equation, Eq. 4, to be solved in these multiple steps without losing accuracy [8, 9]. The durations of the flick and the rest period are correct up to an integer value of the timestep. Finite difference methods are used to discretize Eqs. (6) - (8). The code was written in MATLAB.

To solve for the conservative advection (steps 1 and 4), a third order weighted essentially nonoscillatory method (WENO) was used [10]. WENO methods are designed to handle nonsmooth concentrations and velocity fields better than other numerical methods. Dirichlet boundary conditions were used in the inflow and outflow sections of the domain, Ω. In regions of inflow (on the right wall of the domain), the incoming odor concentration was set to 0 for a thin filament initial condition. For a thick filament initial condition, the incoming concentration was set to the initial maximum value of the concentration, C_∞, when regions of inflow occurred on the right wall. The concentration was set to zero on the other walls. In regions of outflow, only values within the domain were used to compute the boundary data. The outflow boundary conditions were handled as described in [10].

The diffusion step, step 2, was solved using the second order two-dimensional Crank-Nicolson method [11, 12]. No flux boundary conditions were used for a thin filament initial condition. For a thick filament initial condition, no flux boundary conditions were used for all but the right wall during the downstroke. On the right wall during the downstroke, Dirichlet boundary conditions are used, and the concentration is set to the maximum initial concentration value, C_∞. For the return stroke and rest periods, the boundary condition on the right wall is no flux.

Eight different cases were used to quantify the convergence of the method. As the grid resolution for the odor concentration increased and the timestep decreased, convergence was observed for the odor concentration in Ω, in the concentration absorbed by individual aesthetascs, and in the total concentration absorbed by all aesthetascs. The error in the total concentration absorbed by all aesthetascs between consecutive resolutions was approximately 6% in the worst case while in most cases the error was less than 2%. Based on the resolution study, we used spatial grids of 512 or 1024 in the x-coordinate, resulting in a gridsize, h, and then used the same gridsize, h, in the y-coordinate for each simulation. The timestep, dt, was determined by the smaller of the constraint set by the Courant-Friedrichs-Lewy condition ($0.9h/U_\infty$ where U_∞ is the maximum velocity and h is the spatial gridsize) or the constraint set by the diffusive length scale ($R^2/4D$ where R is the radius of the smallest aesthetasc and D is the diffusion coefficient) [12].

Preprocessing of PIV Velocity Fields

The velocity fields (both the downstroke and the return stroke) collected were modified in the following way prior to being used in the numerical simulations as the vector field (u, v):

1. The velocity field was linearly interpolated to the grid upon which the advection-diffusion equation was solved.

2. The velocity at any grid point within a hair was set to 0.

3. We also require that the flow velocity approach zero near the aesthetascs to enforce the no-slip condition. For marine crab simulations, the velocity field was made to smoothly

approach 0 at the boundary of each aesthetasc. This was necessary given the resolution of the PIV data in comparison to the domain size and the size of each aesthetasc. Smoothing was not repeated for the terrestrial crabs because the magnitude of the flow was already small close to each aesthetasc.

For marine crab simulations, this smoothing is done by multiplying the interpolated velocity field by an approximate Heaviside function which is 0 within each aesthetasc and 1 away from each aesthetasc. Close to each aesthetasc, the approximate Heaviside is given by the following equation:

$$H_w(r) = \kappa\left(\frac{2}{Ndx}r - 1\right) \qquad 0 \le r \le Nh \tag{9}$$

where r is the distance from the boundary of the hair in the normal (or radial) direction and

$$\kappa(\xi) = \frac{1}{2}\left(1 + \xi + \frac{\sin(\pi\xi)}{\pi}\right) \qquad -1 \le \xi \le 1\,. \tag{10}$$

The choice $N = 1$ is made to have a smoothing region of one gridsize away from each hair in the radial direction. This choice was made to allow to minimize error while still producing a positive, smooth function [13, 14].

This method of preprocessing the velocity fields was employed to maintain the physical features of the flow field. Experimental limitations also do not allow us to resolve the flows at the resolution needed in the simulations (the resolution needed is detailed above). Therefore, we interpolate from the experimental data to the grids used in the simulations. Other researchers in similar situations, e.g. [15], have also chosen to modify the experimental velocity fields to be divergence free in two dimensions. We have chosen not to perform this modification in order to minimize the processing of the flow fields given that a two-dimensional slice of a three-dimensional flow is not necessarily divergence free.

References

[1] Waldrop, L., Reidenbach, M. & Koehl, M., 2015 Flexibility of crab chemosensory sensilla enables flicking antennules to sniff. *Biological Bulletin* **229**, 185–198.

[2] Waldrop, L. & Koehl, M., 2016 Do terrestrial hermit crabs sniff? air flow and odorant capture by flicking antennules. *J Royal Soc Interface* **13**, DOI: 10.1098/rsif.2015.0850.

[3] Waldrop, L., 2012 *The fluid dynamics of odor capture by crabs.* Ph.D. thesis, University of California, Berkeley.

[4] Waldrop, L., 2013 Ontogenetic scaling of the olfactory antennae and flicking behavior of the shore crab, *Hemigrapsus oregonensis*. *Chemical Senses* **38**, 541–550.

[5] Loudon, C., Best, B. & Koehl, M., 1994 When does motion relative to neighboring surfaces alter the flow-through arrays of hairs. *Journal of Experimental Biology* **193**, 233–254.

[6] Sveen, J., 2004 *An introduction to MatPIV v. 1.6.1: Mechanics and Applied Mathematics.* Dept. of Mathematics, Univ. of Oslo, Oslo, 2nd edition.

[7] Cowen, E. & Monismith, S., 1997 A hybrid digital particle tracking velocimetry technique. *Exp. Fluids* **22**, 199–211.

[8] Strang, G., 1968 On the construction and comparison of difference schemes. *SIAM J. Numer. Anal.* **5**, 506–517.

[9] LeVeque, R. J., 2002 *Finite Volume Methods for Hyperbolic Problems*. Cambridge University Press.

[10] Shu, C.-W., 1997 Essentially non-oscillatory and weighted essentially non-oscillatory schemes for hyperbolic conservation law. Technical report, Institute for Computer Applications in Science and Engineering, NASA Langley Research Center.

[11] Strikwerda, J. C., 2004 *Finite Difference Schemes and Partial Differential Equations*. Society for Industrial and Applied Mathematics.

[12] LeVeque, R. J., 2007 *Finite Difference Methods for Ordinary and Partial Differential Equations*. Society of Industrial and Applied Mathematics.

[13] Sussman, M., Smereka, P. & Osher, S., 1994 A level set approach for computing solutions to incompressible two-phase flow. *Journal of Computational Physics* .

[14] Tornberg, A.-K., 2000 *Interface Tracking Methods with Application to Multiphase Flows*. Ph.D. thesis, Royal Institute of Technology.

[15] Stacey, M. T., Mead, K. S. & Koehl, M. A. R., 2002 Molecule capture by olfactory antennules: Mantis shrimp. *Mathematical Biology* .

[16] Waldrop, L., Bantay, R. & Nguyen, Q., 2014 Scaling of olfactory antennae of the terrestrial hermit crabs *Coenobita rugosus* and *Coenobita perlatus* during ontogeny. *PeerJ* **in press**.

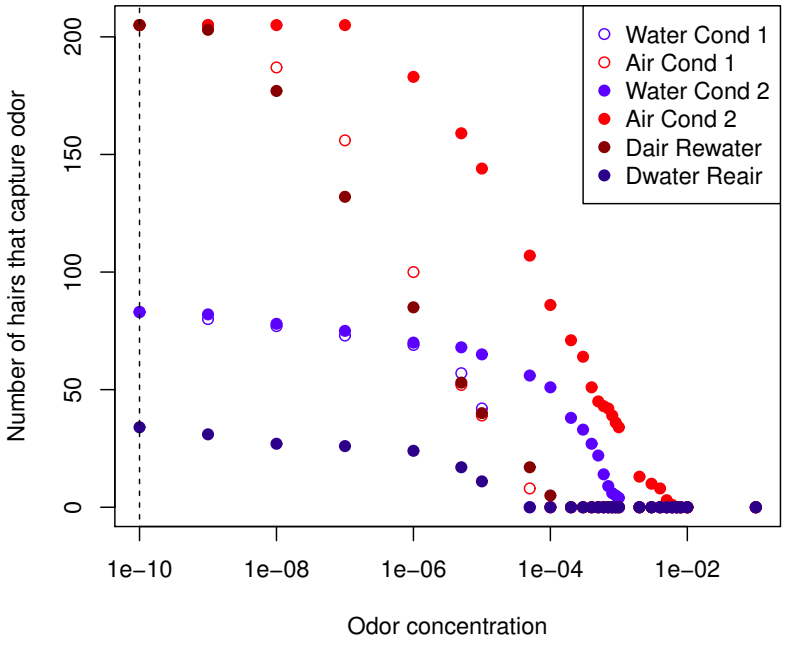

Figure 1: The number of aesthetascs capturing a minimum cutoff of total unadjusted concentration (C) versus minimum concentration cutoff values of C for marine crabs.

Table 1: Values used for creating velocity fields using dynamically scaled physical models of the terrestrial hermit crab, *Coenobita rugosus*. *Using $Re = UL/\nu$, aesthetasc diameter $L = 1.5 \times 10^{-5}$m [16]. † Using $Pe = UL/D$, aesthetasc diameter $L = 1.5 \times 10^{-5}$m [16]

Parameter	Air	Water
Diffusion coefficient, D (m^2s^{-1})	6.02×10^{-6}	7.84×10^{-10}
Kinematic viscosity, ν (m^2s^{-1})	8.50×10^{-6}	1.05×10^{-6}
Downstroke speed, U (m s^{-1})	0.063	0.063
Actual Downstroke Re^{*}	0.11	0.90
Modeled Downstroke Re^{*}	0.098	0.77
Downstroke $Pe^{\dagger}$	0.16	1,200
Return stroke speed, U (m s^{-1})	0.11	0.11
Actual Return stroke Re^{*}	0.19	1.6
Modeled Return stroke Re^{*}	0.21	0.77
Return stroke $Pe^{\dagger}$	0.27	2,100

Table 2: Values used for creating velocity fields using dynamically scaled physical models of the marine blue crab, *Callinectes sapidus*. *Using $Re = UL/\nu$, aesthetasc diameter $L = 9.0\times10^{-6}$m [1]. †Using $Pe = UL/D$, aesthetasc diameter $L = 9.0 \times 10^{-6}$m [1]

Parameter	Air	Water
Diffusion coefficient, D (m^2s^{-1})	6.02×10^{-6}	7.84×10^{-10}
Kinematic viscosity, ν (m^2s^{-1})	8.50×10^{-6}	1.05×10^{-6}
Downstroke speed, U (m s^{-1})	0.17	0.17
Actual Downstroke Re^*	0.18	1.5
Modeled Downstroke Re^*	0.20	1.6
Downstroke $Pe^\dagger$	0.25	2,000
Return stroke speed, U (m s^{-1})	0.061	0.061
Actual Return stroke Re^*	0.060	0.52
Modeled Return stroke Re^*	0.070	0.57
Return stroke $Pe^\dagger$	0.091	700

Captions for attached movies

Movie S1 Terrestrial crab simulation in air (Re_{air}, D_{air}) for a thin filament. This corresponds to the dashed, red line in Fig. 4A in the paper.

Movie S2 Terrestrial crab simulation in air (Re_{air}, D_{air}) for a thick filament. This corresponds to the dashed, red line in Fig. 4C in the paper.

Movie S3 Marine crab simulation in water (Re_{water}, D_{water}) for a thin filament. This corresponds to the solid, blue line in Fig. 4A in the paper.

Movie S4 Marine crab simulation in water (Re_{water}, D_{water}) for a thick filament. This corresponds to the solid, blue line in Fig. 4C in the paper.